Modeling A High Power Density MEMS Magnetic Induction Machine

H. Köşer (*hurkoser@mit.edu*) and J. H. Lang (*lang@mit.edu*)

Microsystems Technology Laboratories, Laboratory for Electromagnetic and Electronic Systems,
EECS Department, Massachusetts Institute of Technology, Cambridge, MA 02139, USA

ABSTRACT

Most micro-scale electric and magnetic machines studied in the last decade lack the power density to support many practical applications. The magnetic induction machine reported here attempts to transcend this practicality barrier by offering power densities in excess of 200 MW/m^3 and efficiencies of up to 50%, while providing more than 10 W of mechanical power. This is a substantial performance increase in MEMS electromagnetic machines studied to date.

Keywords: Power MEMS, Induction Machine, Magnetic Modeling.

1 INTRODUCTION

This paper introduces the very high power density MEMS magnetic induction machine, for use in a micro gas turbine generator for portable electric power generation [1]. It then focuses on modeling the machine, and describes the creation of a fast and accurate analysis tool for determining optimal machine design and performance. Finally, the predicted performance of an initial design is provided; it is significantly better than previously demonstrated MEMS motors [2]-[4].

2 GEOMETRY & ANALYSIS

Macro-scale induction machines generally involve a cylindrically symmetric geometry, with the rotor located concentrically inside the stator. While this configuration is ideal for producing maximum torque for a given volume, it is not feasible to adopt for MEMS machines. MEMS fabrication constraints almost exclusively permit planar geometries. Therefore, the induction machine studied here is necessarily planar, as shown in Figure 1. Here, the rotor stands just above the stator, supported by air bearings [1]. The stator carries two phases, each with one conductor per slot. Four slots are allocated per pole pair, and the phases are displaced from each other by one slot so as to be magnetically orthogonal.

The axial symmetry of the MEMS magnetic induction machine simplifies its modeling by allowing a mapping of each circular cross-section at a given radius into Cartesian coordinates, as shown in Figure 2. The modeling then proceeds by developing two-dimensional boundary layer solutions of Maxwell's Equations for the rotor, and a magnetic circuit analysis of the stator.

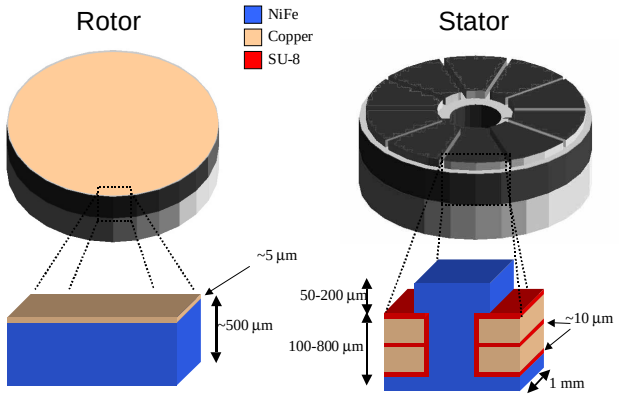

Figure 1: Rotor and stator of a typical MEMS magnetic induction machine, with approximate design dimensions; end-turns not shown.

2.1 Rotor Model

Figure 3 shows a cross-section of the rotor. For this geometry, the boundary conditions relating the tangential magnetic field H_x and normal flux density B_y at surfaces 1 through 8 are

$$\begin{array}{ll} H_{1,x} = H_{ST}\,(x,t) & B_{8,y} = 0 \\ H_{2,x} = H_{3,x} & B_{2,y} = B_{3,y} \\ H_{4,x} = H_{5,x} & B_{4,y} = B_{5,y} \\ H_{6,x} = H_{7,x} & B_{6,y} = B_{7,y} \end{array} \qquad (1)$$

Here, H_{ST} is the tangential field at the stator surface. Because the stator and its excitation are periodic in space and time, H_{ST} can be expanded in Fourier series

$$H_{ST}\,(x,t) = \sum \hat{H}_{ST_m} e^{j(\omega t - kmx)} \qquad (2)$$

where each term in (2) is an orthogonal, traveling wave mode. Note that $k = p/r$, where r is the radius and p is the number of pole pairs of the machine. With this expansion, the rotor geometry can now be analyzed one mode at a time using the equations of magnetic diffusion in moving media [5]. Applying these equations to each

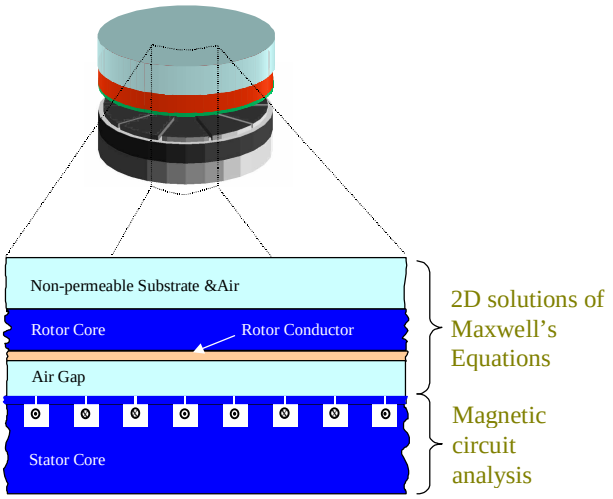

Figure 2: The modeling approach.

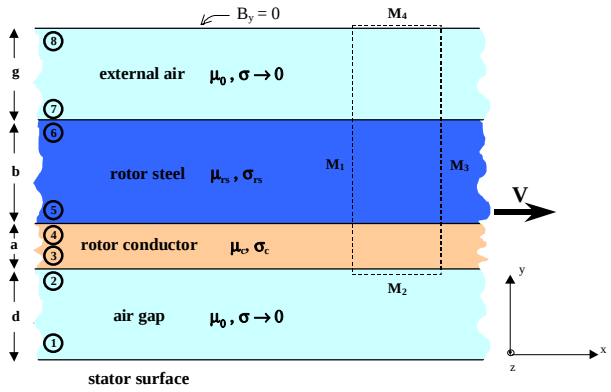

Figure 3: The geometry and properties of the multilayered rotor. The top air layer extends to infinity.

layer in Figure 3 yields

$$\begin{bmatrix} \hat{B}_{1,y} \\ \hat{B}_{2,y} \end{bmatrix} = F\left(\gamma_0 d, \frac{jk\mu_0}{\gamma_0}\right) \begin{bmatrix} \hat{H}_{ST} \\ \hat{H}_{2,x} \end{bmatrix} \quad (3)$$

$$\begin{bmatrix} \hat{B}_{3,y} \\ \hat{B}_{4,y} \end{bmatrix} = F\left(\gamma_c a, \frac{jk\mu_c}{\gamma_c}\right) \begin{bmatrix} \hat{H}_{3,x} \\ \hat{H}_{4,x} \end{bmatrix} \quad (4)$$

$$\begin{bmatrix} \hat{B}_{5,y} \\ \hat{B}_{6,y} \end{bmatrix} = F\left(\gamma_{rs} b, \frac{jk\mu_{rs}}{\gamma_{rs}}\right) \begin{bmatrix} \hat{H}_{5,x} \\ \hat{H}_{6,x} \end{bmatrix} \quad (5)$$

$$\hat{B}_{7,y} = -j\mu_0 \hat{H}_{7,x} \quad (6)$$

Here, $\gamma_i = \sqrt{k^2 + j\mu_i\sigma_i(\omega - kV)}$, where i is the layer index, and $F(\alpha,\beta) = \beta \begin{bmatrix} -\coth(\alpha) & \frac{1}{\sinh(\alpha)} \\ -\frac{1}{\sinh(\alpha)} & \coth(\alpha) \end{bmatrix}$. Finally, Equations (1)-(6) are solved for each traveling wave mode to determine the complex magnetic field and flux density amplitudes at each boundary surface as a function of $\hat{H}_{ST_m}$.

2.2 Time-average Force

The x-directed shear and y-directed pull-in force densities acting on the rotor are obtained by integrating the Maxwell Stress Tensor [5] over the surface M_1 through M_4 of Figure 3. This yields

$$\langle \tau_{xy} \rangle_t = \sum_m \frac{\mu_0}{2} \mathrm{Re}\left\{ \hat{H}_{2,x_m} \hat{H}^*_{2,y_m} \right\} \quad (7)$$

$$\langle \tau_{yy} \rangle_t = \sum_m \frac{\mu_0}{4} \mathrm{Re}\left\{ \hat{H}_{2,y_m} \hat{H}^*_{2,y_m} - \hat{H}_{2,x_m} \hat{H}^*_{2,x_m} \right\} \quad (8)$$

Due to modal orthogonality, the contributions to the stresses on the rotor from each mode number (as denoted by the index m) are independent of the rest. This permits the simple summation of each contribution in Equations (7) and (8) to determine the total stresses for a given radius. These stresses are integrated over the rotor radius to yield torque and pull-in force.

2.3 Stator Model

The stator is spatially non-uniform, with features such as pole teeth, wire slots, etc. Hence, the stator is most easily modeled using magnetic circuits. Figure 4 shows the circuit used here.

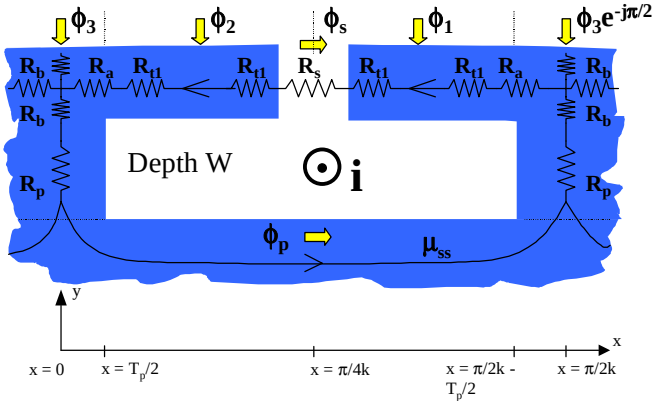

Figure 4: Magnetic circuit of the stator. The current, i, passing through the wire slot is the sum of the currents in the two phases.

Following the model in Figure 4, the flux components entering the stator for each mode can be expressed as

$$\phi_{1_m} = \int_{\frac{\pi}{4k}}^{\frac{\pi}{2k} - \frac{T_p}{2}} -\hat{B}_{1,y} e^{j(\omega t - kmx)} W dx$$

$$\phi_{2_m} = \int_{\frac{T_p}{2}}^{\frac{\pi}{4k}} -\hat{B}_{1,y} e^{j(\omega t - kmx)} W dx$$

$$\phi_{3_m} = \int_{-\frac{T_p}{2}}^{\frac{T_p}{2}} -\hat{B}_{1,y} e^{j(\omega t - kmx)} W dx$$

With these flux components and the current i as sources within the magnetic circuit model, the model can be readily analyzed to yield

$$\phi_{s_m} = \frac{\begin{array}{c}\left(R_{t1}+R_a+\left(1-e^{\frac{-j\pi}{2}}\right)(R_b+R_p)\right)\phi_{1_m} \\ +\left(\left(e^{\frac{j\pi}{2}}-1\right)(R_b+R_p)-(R_{t1}+R_a)\right)\phi_{2_m} \\ +\left(\left(1-e^{\frac{-j\pi}{2}}\right)(R_b+R_p)\right)\phi_{3_m}-i\end{array}}{4R_{t1}+R_s+2R_a+2R_b+2R_p} \tag{9}$$

where ϕ_s is the lateral flux between stator teeth near the stator surface. Ideally, ϕ_s as given by Equation (9) is the dominant factor that determines H_{ST}. This is because air will have a much lower magnetic permeability than the stator steel; hence, the gap between the teeth will have the highest reluctance, resulting in the highest mmf drop anywhere in the magnetic circuit. However, for configurations in which the stator steel has a relatively low magnetic permeability, mmf drops along the teeth contribute to H_{ST} as well. Therefore, in the most general case, all x-directed flux along each tooth surface must be considered as contributing to H_{ST}.

Figure 5 shows an example of how the x-directed flux along the top of the stator contributes to H_{ST}. Note that the figure spans one quarter of a pole pair. The

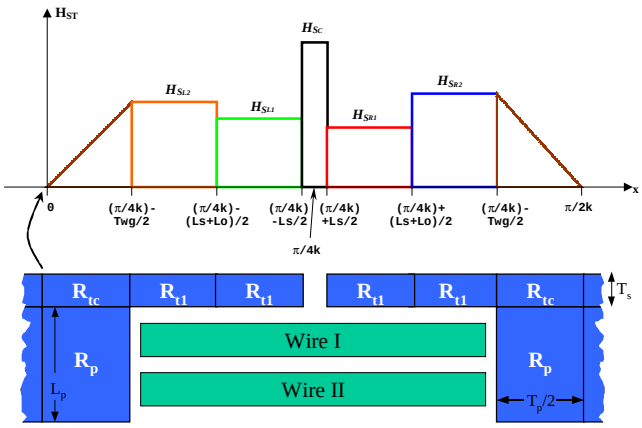

Figure 5: Depiction of tangential magnetic field just over the stator along one wire slot.

height of each rectangle in Figure 5 is proportional to the flux density through the corresponding section of the magnetic circuit, and is given by

$$H_{S_c} = \frac{\phi_s}{\mu_0 T_s W} \qquad H_{S_{R1}} = H_{S_{L1}} = \frac{\phi_s}{\mu_{ssg} T_s W}$$
$$H_{S_{R2}} = \frac{\phi_s + \phi_2}{\mu_{ssg} T_s W} \qquad H_{S_{L2}} = \frac{\phi_s - \phi_1}{\mu_{ssg} T_s W}$$

The approximation that the x-component of the flux along the corner reluctance R_{tc} decays linearly, as shown on either edge of the plot in Figure 5, is a good one, as justified later with comparisons to FEA results.

Decomposing H_{ST} into its Fourier series yields $\hat{H}_{ST_m}$ of Equation (2), thereby completing the coupling between the rotor and the stator models.

3 MODEL IMPLEMENTATION

The equations derived above, as well as other performance criteria such as heat dissipation in the windings, core losses in the steel, windage losses and magnetic saturation have been implemented in a software analysis tool. The backbone of this tool has been programmed in C for speed, whereas the user interface and data analysis is inside the $MATLAB^{TM}$ environment for convenience. The graphical user interface allows the designer to select various geometries for the entire magnetic machine, as well as material properties, operating temperature, number of poles, and other machine parameters.

3.1 FEA Studies

A commercially available FEA package ($Maxwell^{TM}$) has been used to study various micromotor geometries. This software provides the capability to examine a great variety of electromagnetic phenomena, including eddy current effects and magnetic diffusion. Therefore, it is an ideal tool for investigating magnetic induction machines. Nevertheless, it is not practical to design the entire machine on $Maxwell^{TM}$; as with many other powerful FEA packages, simulations simply take too long. This is especially the case for the planar MEMS geometry, where thin but wide structures necessitate very fine meshing for accuracy.

The FEA software has been used exclusively for validating the model. For the case of a very large steel magnetic permeability, the model and the FEA results are indistinguishable. Initial measurements indicate that over the frequency ranges of interest, the relative permeability of the NiFe steel is in excess of 1000. Yet, comparisons between results of the two tools have been made for relative permeabilities down to 50, and the worst case discrepancy in stress has been found to be less than 5%, as Figure 6 shows.

It is important to note that the frequency of peak τ_{xy} is calculated accurately in the model. The small discrepancy is mainly due to overestimating the magnetic reluctance at the stator teeth corners, the value of R_{tc} in Figure 5. A conformal mapping method (Schwarz-Christoffel Transformation) has been employed to compute the reluctance of the corner sections where flux lines bend; this approach has further reduced the worst-case error shown in Figure 6 to less than 1%.

In summary, the design tool based on our model is not only very fast and practical, but also is robust to permeability and geometry variations. The agreement

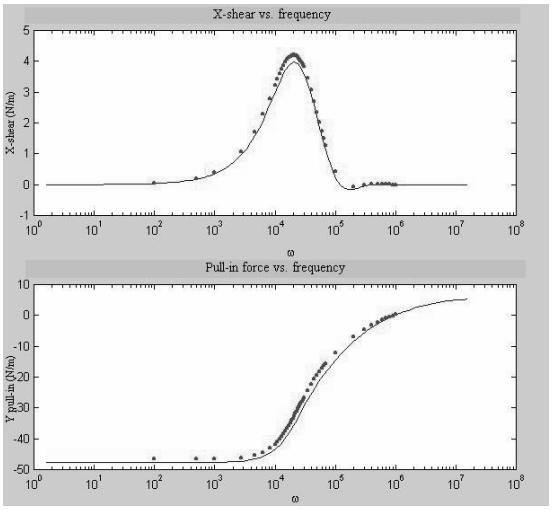

Figure 6: Tangential shear stress (above) and vertical pull-in pressure (below) vs. rotor slip frequency, at a given r, for low permeabilities ($\mu_{rs} = 50$, and $\mu_{ss} = 100$). The solid lines correspond to the model predictions, where as the points are FEA results for the same geometry.

with the FEA and the design tool results is excellent. The $MATLAB^{TM}$ user interface and analysis functions allow designs to be completed in a matter of a few days.

3.2 Initial Designs

Using the design tool described above, a first generation of MEMS magnetic induction machines have been designed. Care has been taken to keep NiFe cores from saturating, which leads to somewhat pessimistic performance estimates. Nevertheless, this approach simplifies validating our model with experiments. Figure 7 presents some performance assesments based on our design tool, and on what is achievable using currently established MEMS fabrication techniques [9].

4 SUMMARY AND CONCLUSIONS

A modeling tool for a magnetic induction machine used as a power MEMS device has been presented. This machine comprises a distributed model for the rotor, and a lumped-parameter magnetic circuit for the stator. A natural splice can be made between the distributed model and the magnetic ciruit approach via Fourier decomposition of the fields at the rotor/stator boundary. Schwarz-Christoffel Transformations have proven very convenient in determining magnetic reluctances. The entire model and analysis tool has been efficiently implemented via C and $MATLAB^{TM}$, and successfully verified using a FEA package. Finally, we conclude that the MEMS magnetic induction machine reported here is an

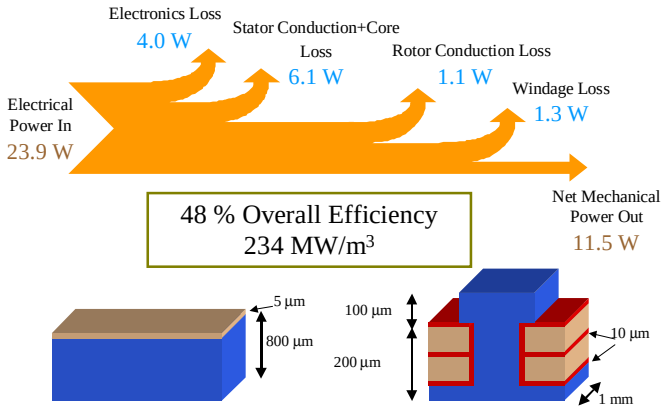

Figure 7: Typical micromotor dimensions achievable today, and various performance criteria, for $\mu_{rs} = \mu_{ss} = 1000\mu_0$, and the design speed of 2.4 million rpm.

excellent candidate for an efficient, high power density MEMS generator/motor.

5 ACKNOWLEDGMENTS

This work is supported by ARO grant DAAG55-98-1-0292, Dr. Thomas L. Doligalski, scientific officer.

REFERENCES

[1] *Epstein, A. H., et al., "Power MEMS and Microengines", IEEE Conf. Solid State and Actuators, June 1997*

[2] *Nagle, S. F., and Lang, J. H., "A Micro-Scale Electric-Induction Machine for a Micro Gas Turbine Generator", Proc. ESA Annual Meeting, 1999*

[3] *Guckel, H., et al., "Fabrication and Testing of the Planar Magnetic Micromotor", Micromechanics and Microengineering, pp. 135-138, vol. 1, 1991*

[4] *Mehregany, M., et al., "A Study of Three Microfabricated Variable-capacitance Motors", Sensors and Actuators, pp. 173-179, A21-A23, 1990*

[5] *Melcher, J. R., "Continuum Electromechanics", Table 6.5.1, pp. 6.12, MIT Press, 1981*

[6] *Churchill, R. V., "Complex Variables and Applications", pp. 171-187, McGraw-Hill, 1948*

[7] *Balakrishnan, A., et al., "Air-Gap Reluctance and Inductance Calculations for Magnetic Circuits Using a Schwarz-Christoffel Transformation", IEEE Trans. Power Elec., Vol. 12, No. 4, 1997*

[8] *Driscoll, T. A., Schwarz-Christoffel Toolbox User's Guide*

[9] *Cros, F., and Allen, M. G., "High Aspect Ratio Structures Achieved by Sacrificial Conformal Coating", Proc. IEEE Solid-State Sens. Act. Workshop, 1998*